Toward real-time shear-wave imaging: Ultradense magnetic sources enable rapid diffuse field correlations

G. Laloy-Borgna, B. Giammarinaro, Z. Sun, S. Catheline, J. Aichele

Towards real time shear wave imaging: Ultra-dense magnetic sources enable rapid diffuse field correlations

Laloy-Borgna G.,[1,2] Giammarinaro B.,[1,*] Sun Z.,[3] Catheline S.,[1] and Aichele J.[1,4,†]

[1]*Laboratory of Therapeutic Applications of Ultrasound, INSERM & University of Lyon, Lyon, France*
[2]*Department of Imaging Physics, Delft University of Technology, 2628 CJ Delft, The Netherlands*
[3]*College of Information and Communication Engineering, Faculty of Information Technology, Beijing University of Technology, Beijing, China*
[4]*Department of Earth Sciences, Institute of Geophysics, Swiss Federal Institute of Technology, Zürich, Switzerland*

(Dated: November 23, 2024)

Perfectly diffuse wavefields are the underlying assumption for noise correlation tomography in seismology, non-destructive testing and elastography. However, perfectly diffuse fields are rarely encountered in real world applications. We show that homogeneously distributed magnetic microparticles allow to instantaneously generate a diffuse wavefield, which is imaged using a clinical probe connected to a fully-programmable ultrasound scanner. The particles are placed inside a bi-layered hydrogel and act as elastic wave sources on excitation by a magnetic pulse. Using ultrafast ultrasound imaging coupled to phase tracking, the diffuse elastic wave-field is imaged. This allows measuring the local wave velocity everywhere on the image through noise-correlation algorithms inspired by seismology. Thanks to this instantaneous diffuse wavefield, a very short acquisition time is sufficient to retrieve the wave speed contrast of the bilayered phantom. The correlation time window can be shrunk down to 3 time samples, which we show in a numerical simulation mimicking the experimental conditions. Our experimental and numerical results are consistent with theoretical predictions made by information theory, and pave the way for real-time elasticity imaging. This is of particular interest for medical treatment monitoring through real-time tissue elasticity assessment, and is applicable in related fields such as seismology or non-destructive testing.

I. INTRODUCTION

Passive imaging methods are based on the extraction of information from random wave-fields, naturally occurring within the body of interest. Thus, imaging is possible without the need for precisely controlled sources by exploiting rather than suppressing what is commonly called "noise". In the context of elastic waves, passive imaging methods are widely applied in global and environmental seismology, seismic exploration, non-destructive testing and medical imaging.

Examples include seismic interferometry [1, 2], noise or coda correlation for earthquakes [3] and icequakes [4], synthetic wave lamb focusing in Non-Destructive Testing (NDT) [5] and passive seismic tomography [6] for reservoir monitoring. In medical imaging for tissue stiffness estimation, passive elastography exploits the shear wave fields naturally present in the human body. Herefore, a shear wave speed map is retrieved from the correlation of ultrasound (US) [7, 8], magnetic resonance (MRI [9]) or optical ([10, 11]) images. The imaged shear wave field commonly results from the cardiac activity, arterial pulsatility or muscle activity. A comprehensive review of the different passive elastography algorithms was recently published [12].

Extracting information from noise through cross-correlation is closely related to time reversal [13]. It relies on source-receiver reciprocity [14] to retrieve the exact impulse response or Green's function between two points. The method is based on the assumption that the wavefield is diffuse, which means that at each location and frequency it is an "isotropic random superposition of plane waves" [15]. This is achieved through homogeneous sources distribution or multiple scattering. The first experimental proof employed scattered thermal fluctuations of ultrasonic fields in an aluminium cylinder [16]. Homogeneous source distributions are rarely considered due to difficulties in experimental realization [17], and issues arising when sources inside the Region-of-Interest contribute [18, 19]. Experimental realization of homogeneous source distributions is facilitated if the sources can be activated remotely, as is the case for magnetic particles.

Bio-compatible magnetic nanoparticles are widely used as contrast agents in magnetic resonance imaging [20, 21], are emerging in the field of magnetic particle imaging [22] and cancer treatment [23]. They have been used in vivo for magneto-motive ultrasound imaging [24] and clustered magnetic nanoparticles previously acted as a shear wave source for transient elastography [25]. In a recently published paper, we showed that homogeneously distributed magnetic nanoparticles excited by a magnetic pulse can act as shear wave sources in cell aggregates [26]. Assuming that dispersed mag-

* bruno.giammarinaro@inserm.fr
† johannes.aichele@rwth-aachen.de

netic micro-particles excited by a pulsed magnetic field can act as shear wave point sources, a magnetic excitation of a magnetic hydro-gel would lead to the instantaneous generation of a diffuse shear wave field.

We present an experimental proof-of-concept for real-time magnetic elastography, which combines passive elastography imaging and a magneto-motive material made of dispersed magnetic micro-particles. The instantaneous generation of a diffuse wave-field allows us to shorten the correlation time needed to retrieve an elasticity contrast. We then show numerically that the imaging window can be shrunk down to three time samples for an ideal source distribution. This is consistent with the theoretical minimum predicted by Gabor information theory.

II. DIFFUSE FIELD EXPERIMENT

A. Experimental setup

a. Bi-layered phantom fabrication. First, we created a bi-layered elastic phantom consisting of gelatin powder (gelatin from porcine skin, G2500 Sigma-Aldrich, Burlington, Massachusetts, USA), xanthan gum (Meilleur du Chef, Bassussarry, France) and magnetic micro-particles (Iron (II,III) oxide <5 µm, 310069 Sigma-Aldrich, Burlington, Massachusetts, USA). The gelatin and xanthan powder were incorporated in warm water (90 °C), using concentrations of 0.25 % of xanthan (i.e. 0.25 g of xanthan for a 100 mL solution), and 4 and 10 % of gelatin. Then, 1 % of micro-particles were added, and the solution was mixed using a vibrating plate. The phantom was cooled down at 4 °C until complete gelation. To obtain a bi-layered phantom of varying stiffness, the softer layer (4 % of gelatin) was first poured and gelled. In a second step, the other layer (10 % of gelatin) was poured on top of the first one and gelled.

b. Magnetic pulse excitation. As depicted in figure 1(a), the solidified gel was placed inside a coil connected to a home-made magnetic pulser [27]. The magnetic pulse was created by the discharge of a 6 µF capacitor charged by a 5 kV voltage in a 173 µH coil, which resulted in a 0.2 ms magnetic pulse of 250 mT in air. Note that the presence of paramagnetic particles leads to a higher field inside the sample. The gel was solidified without application of a magnetic field, and the magnetic particles should thus be distributed without a preferred orientation. Under the pulsed magnetic field, the magnetic particles aligned along the magnetic field lines. As a result, a particle displacement or rotation was created on each single micro-particle. Because the magnetic particles were likely bound to the gelatin fibers by adhesive forces [28], the particle movement exerted a force on the elastic gel. Finally, each particle acted as an elastic wave source of random directionality.

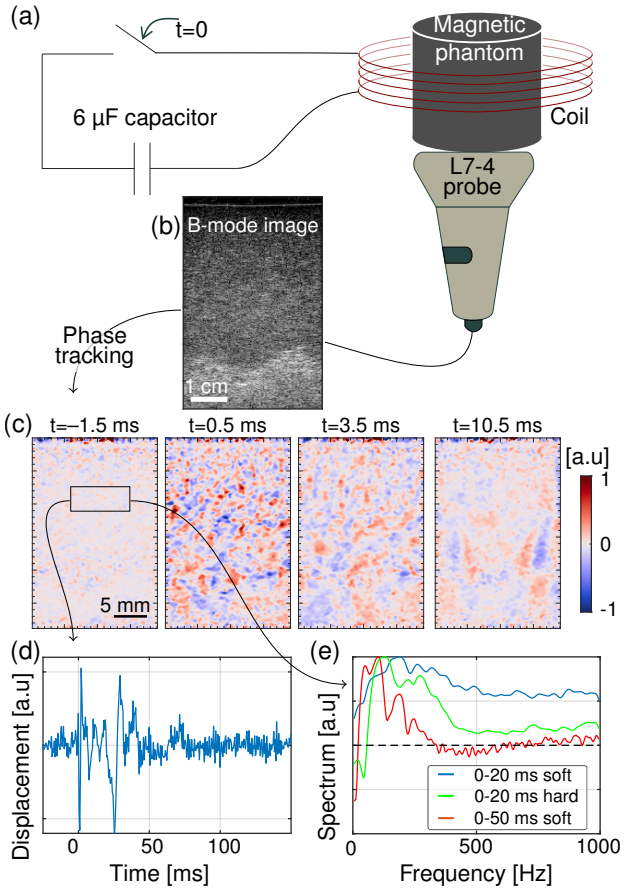

FIG. 1. **Schematic experimental setup and imaging method.** (a) A simplified electrical layout used to generate the magnetic pulse. (b) Example of an ultrasound backscatter (B-mode) image. (c) Exemplary snapshots of the axial particle velocity field at −1.5, 0.5, 3.5 and 10.5 ms, t=0 being the start of the 0.2 ms magnetic pulse. (d) Time signal spatially averaged on the box depicted in figure (c). (e) Averaged spectral content of the wave-fields for three different time-windows, either in the soft (top) or in the stiff (bottom) layer. Dotted black line: amplitude of -10dB.

c. Ultrasound imaging. The bi-layered sample was imaged using a clinical L7-4™(Philips ATL Bothell, WA, USA) ultrasonic probe connected to a fully-programmable ultrasound scanner (Verasonics Vantage™, Kirkland, WA, USA). The scanner and magnetic pulser were synchronized in order to retrieve the shear wave field during and after the magnetic excitation. Plane ultrasound waves were transmitted at three different angles from the 128 element array at a Pulse Repetition Frequency (PRF) of 6000 Hz.

d. Noise correlation shear wave elastography. The compounding method [29] was applied to combine three low-quality images (one for each plane wave angle) in order to obtain a single high-quality image (see fig-

ure 1(b)). Overall, the frame rate was 2000 Hz. In addition, since a ultrasonic Speckle is created by the magnetic micro-particles, local motion can be tracked inside the phantom by measuring the displacement of the pattern that can be seen in figure 1(b). To this purpose, a phase-based motion estimator [30] was applied to the beam-formed IQ data of the backscattered US images to retrieve the axial particle velocity field u_z (vertical axis on the figures). Finally, the shear wave speed map was retrieved using noise correlation algorithms, based on a cross-correlation method applied to the shear wave field [7, 8, 31, 32]. Here, the local shear wave speed is estimated as follows [32]:

$$c_s = \frac{\omega}{k} \cong \sqrt{\frac{1}{5}\frac{V^{TR}}{\xi^{TR}}} \text{ with } V^{TR} = \frac{\partial u_z}{\partial t}(-t) \otimes \frac{\partial u_z}{\partial t}(t) \text{ and } \xi^{TR} = \frac{\partial u_z}{\partial z}(-t) \otimes \frac{\partial u_z}{\partial z}(t) \quad (1)$$

where ω is the angular frequency, k the wave vector, z the spatial vertical coordinate and t the temporal coordinates. TR stands for Time-Reversal, and V^{TR} and ξ^{TR} are the time-reversed particle velocity and strain fields. The algorithm temporally cross-correlates displacement signals between measurement points. At time lag zero, called the refocusing time, the cross-correlation of one measurement point with all other points leads to a focal spot. The curvature of the focal spot at one point is directly linked to the shear wavelength at this precise location [32]. It is worth mentioning that there is no spatial correlation mentioned here, both the estimations of the central wavelength and period are based on temporal cross-correlations between displacement signals. Initially, equation 1 was developed for diffuse wave fields detected in passive elastography. Since then, it was shown that noise correlation elastography can also be applied to a non-diffuse wave field [33]. However, since a non-diffuse wave field is not ideal for noise correlation algorithms, longer correlation windows are likely to be necessary in order to retrieve the local wavelength from the focal spot.

B. Towards real-time elastography: retrieving an elasticity contrast in 20 ms

Snapshots of the acquired particle velocity field are coded in red and blue and displayed in figure 1(c) at four time points, before and after the magnetic excitation (beginning at $t = 0$ and ending at $t = 0.2$ ms). It can be seen that a non-directional diffuse wave field was created by the pulsed magnetic field. This wave source is likely to generate compressional waves too, which propagate about 1000 times faster than shear waves in this quasi-incompressible medium, hence they travel about one meter in between two frames and are rapidly attenuated. In addition, compression wave amplitudes in soft tissues are smaller than shear wave amplitudes, which is why they are routinely ignored in ultrasound elastography. An assumption we also make throughout this paper. The spatial average of the signal on a small region is plotted in figure 1(d). It contains high frequency elastic waves with significant spectral content above 500 Hz, as shown in fig.1(e). The high frequencies are only detectable at early times due to rapid attenuation, as expected for visco-elastic solids. However, this strong attenuation due to the presence of high frequencies is not an issue since the sources are spread out everywhere in the imaged medium and the medium is thus spatially covered with high frequency wave propagation.

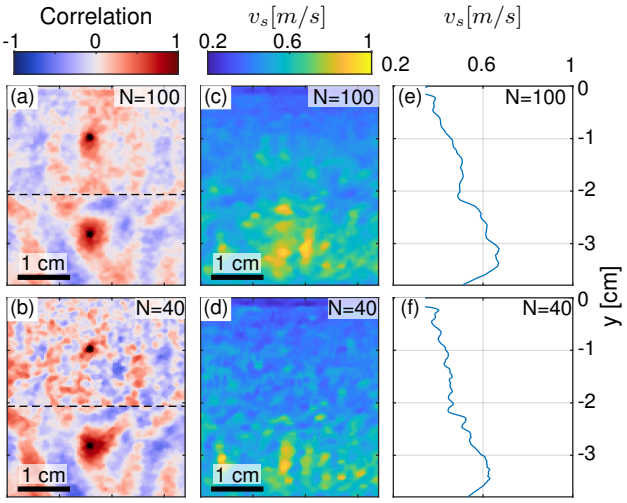

FIG. 2. **Noise-correlation elastography results.** (a)-(b) Two focal spots calculated in each of the two elastic layers using (a) 100 snapshots (50 ms) and (b) 40 snapshots (20 ms) of displacements. (c)-(d) Shear wave speed maps retrieved using noise-correlation elastography algorithm when considering (c) 100 and (d) 40 snapshots. (e)-(f) Velocity profiles retrieved by averaging along the x-axis the speed maps shown in (c) and (d).

To retrieve the wave speed contrast, a noise correlation algorithm is applied to the generated elastic wavefield of fig.1. First, focal spots were calculated, and are shown in figures 2(a) and (b). Figure 2(a) shows two focal spots at two points in the top and bottom layers marked by black stars, calculated using a 100 time step (50 ms) window. The wider focal spot in the bottom layer corresponds to a larger shear wavelength, which indicates a higher shear wave velocity. This agrees with the bottom layer being stiffer than the top one in the fabrication process. Figure 2(b) shows the same focal spots but for a 40 time points (20 ms) window. The width difference between the two focal spots is conserved, but with a lower signal-to-noise ratio.

Second, figures 2(c) and (d) show the shear wave velocity maps retrieved using the noise correlation algorithm summarized in equation 1. Figure 2(c) is obtained using the same 100 snapshots as above, and 2(d) using only 40 snapshots. Both wave velocity maps show a layering of the gel, which is confirmed by the horizontally averaged wave velocity profiles, plotted in figures 2(e) and (f). To confirm the elasticity layering of the phantom, we also performed an independent measurement using Acoustic Radiation Force Impulse - Shear Wave Elastography (ARFI-SWE), the gold-standard. The results results are presented in the Appendix. The slower top layer (low gelatin concentration) is separated from the faster bottom layer (high gelatin concentration) at $\simeq 22\,\mathrm{mm}$, which coincides with interface depth found using ARFI-SWE. Hence, the analysis of a high frequency wave-field on 40 snapshots over 20 ms immediately after the magnetic pulse is sufficient to retrieve an elasticity contrast. Coupled to a fast data processing algorithm, this type of experiment could allow measuring tissue elasticity in real time. We explicitly choose to present wave speed values and not shear moduli since wave speed is the data observable. Conversion to Moduli would require an inversion through the application of a rheological model.

Quantitatively, the results for different correlation windows differ. The shortest window, which contains the highest frequency content, results in a 20 % (measured at 35 mm depth) higher speed profile than the longest window. Gelatin gels are strictly speaking not purely elastic but visco-elastic [34, 35], hence the shear wave speed increases with frequency. The shorter correlation window directly follows the magnetic impulse and exposes higher frequencies than later windows (see fig. 1(c)). Thus, the longer time window gives more weight to the lower, and thus slower, frequencies. The effect only becomes clearly apparent in the stiffer (lower part) of the gel. We attribute this to an increased gelatin percentage in the lower gel, which likely results in a higher viscosity.

Using a magnetic stimulation impulse, we managed to retrieve a shear wave velocity map by analysing 40 ms of acquisition only. However, the achievable temporal resolution in our magneto-motive experiment is limited by several factors: the access to a single component of the 3D particle velocity field, the quantity and distribution of magnetic particles and their adherence to the gelatin fibers. In order to test the minimum number of time samples needed to retrieve an elasticity contrast, we used a 2D linear elastic simulation.

III. DIFFUSE FIELD SIMULATION

A. Idealized 2D numerical experiment

We set up a 2D linear elastic spectral element simulation (SALVUS package [36]) in a bi-layered soft tissue phantom. Both layers exhibit the same density ($980\,\mathrm{kg\,m^{-3}}$), and compression wave speed ($1500\,\mathrm{m\,s^{-1}}$), but a shear wave speed contrast shown in figure 3(a): $1\,\mathrm{m\,s^{-1}}$ for the top layer and $2\,\mathrm{m\,s^{-1}}$ for the bottom layer. 30000 randomly polarized directional elastic point forces, required for exact Green's function retrieval [18], are randomly distributed in the Region-of-Interest (ROI) of the medium. They generate each a Ricker (Mexican hat) shaped pulse centered at 300 Hz. The boundary conditions are rigid on the edges of the medium, but boundary reflections do not reach the ROI during simulation time. The elastic wave propagation following the sources excitation is displayed by four snapshots of the resulting particle velocity field in fig. 3(c). A diffuse displacement field containing waves propagating in all directions, without mode development, can be seen. The frequency content of this displacement is presented in fig. 3(b). The spectrum is consistent with the excitation, and stable, proving that the propagation is mode-free.

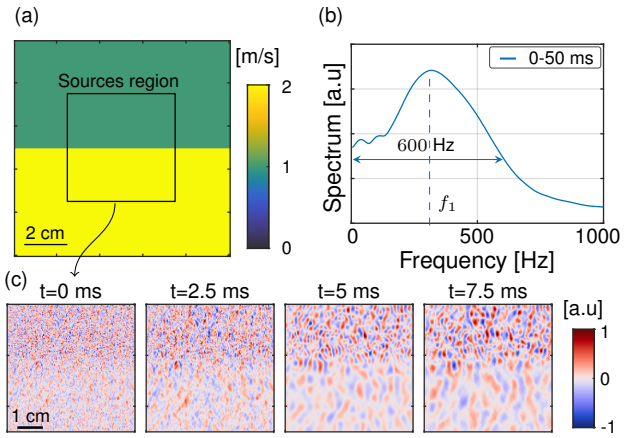

FIG. 3. **Spectral element simulation.** (a) Shear wave map of the bi-layered medium. (b) Spectrum of the shear wave field in the soft region. (c) Snapshots of the displacement field at four time points after the source excitation.

B. Results

Two focal spots equivalent to fig. 2(a-b) are presented in fig. 4(a-b), by using 100 and 3 time steps, respectively. The lower focal spot is larger than the upper one, revealing a larger shear wavelength and velocity for the bottom layer. Analysing 100 snapshots with noise correlation elastography (eq. 1), the wave speed map presented

in fig. 4(c) is obtained. It clearly shows a speed contrast between the two layers of the medium, revealing again a faster, stiffer medium in the bottom layer. The average wave speed profile along depth in 4(e) displays a clear velocity step at the expected depth.

Since a diffuse wave-field is the ideal case for noise correlation algorithms, the minimum window length required can be investigated using this simulated dataset. The convolution in eq. 1 leads to a secondary time derivative and therefore three time steps (frames) are the minimal mathematical requirement of the algorithm. The results of noise correlation obtained using only 3 time states are shown in fig. 4(b-d-f). In fig. 4(d), the two layers are less homogeneous than in 4(c), but a clear wave velocity contrast is still retrieved. This is confirmed by the wave velocity profile shown in 4(f). The numerical simulation thus shows that numerous randomly distributed and orientated sources allow retrieval of a wave velocity contrast with the theoretical minimal time samples number: three.

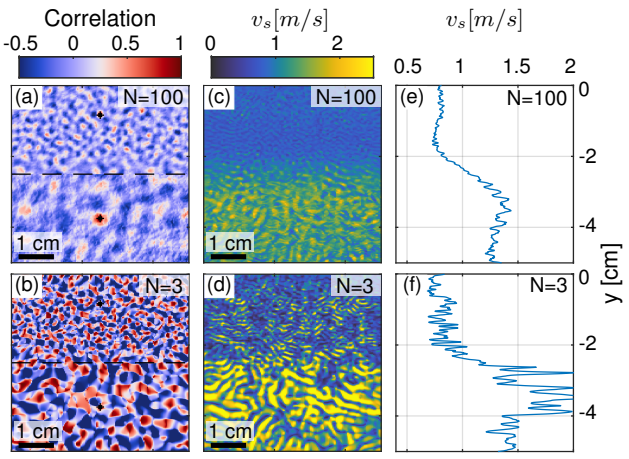

FIG. 4. **Simulation: noise correlation elastography results.** (a)-(b) Two focal spots calculated in each of the two layers retrieved using either 100 (a) or 3 (b) time points are merged together. (c)-(d) Shear wave speed maps retrieved through the correlation method, using either 100 (c) or 3 (d) displacement frames. (e)-(f) Velocity profiles retrieved by averaging along the x-axis of (c)-(d).

IV. DISCUSSION AND PERSPECTIVES

Our results show that a qualitative shear wave speed mapping in real time is possible. Only 40 snapshots (20 ms) of the displacement field are required to achieve shear wave speed contrast imaging in our diffuse field experiment. Theoretically, under ideal conditions, the contrast of the bi-layered phantom could be retrieved by using only 3 snapshots, as shown in our numerical experiment. In the following we discuss the conditions required to retrieve shear wave speed contrast by using a certain number of snapshots.

A. Link with Gabor's information theory

Since the correlation methods used in this paper are inspired from seismology [1–4, 6], the temporal resolution of the method is rarely investigated. Indeed, in seismology the correlated time windows can go to up to one month. However, in medical imaging, real-time imaging modalities are pursued since the medium can be changing quite fast, for example in the context of treatment monitoring. This is why the application of noise correlation techniques to medical imaging leads to new questions such as the maximum imaging frequency achievable. However, it is well established that the longer the correlation window, the better the reconstructed wave speed map. In the words of Gabor's information theory [37–41], longer time windows contain more time-information grains, where an information grain is the basic information unit. Our two key-questions for correlation applied to medical imaging thus are:

- How many information grains does an arbitrary correlation time window contain?
- What is the shortest time window that can be used for correlation?

On the one hand, the number of time-information grains N_T contained in a time window can be calculated through Gabor's uncertainty relation. It is the product of the frequency bandwidth and the window duration: $N_T = \Delta t \Delta f$ [37]. On the other hand, for a certain number of time-information grains, the contrast of the focal spot is given by $\gamma^{corr} = \sqrt{N_T}$, the contrast being defined as the ratio between the focal spot peak amplitude and its standard deviation. If the noise correlation that we use to retrieve focal spots and the wave speed maps obey Gabor's theory, then we have $\gamma^2_{corr} = \Delta t \Delta f$.

In the magneto-motive experiment, the 20 ms time-window having a $\simeq$1000 Hz bandwidth (blue curve of fig.1(d)) correspond to 20 time-information grains. On the other hand, the focal spot contrast of the soft layer in fig. 2(b) is $\gamma^{corr} = 5.15$, which leads to 26 measured time-information grains. The same calculations in the stiff region give a contrast of 3.7 corresponding to 13.6 time-information grains, which is in agreement with a shorter bandwidth (green curve of fig. 1(d)). Similarly, in the 2D elastic simulation, the correlation window lasting 50 ms having a 600 Hz frequency bandwidth contains 30 time-information grains, leading to a contrast of 5.7 (in the soft region of fig. 4(a)). Since $5.7^2 = 33$, the two values are compatible. Hence, there is a very good agreement between the number of time-informations grains

theoretically contained in a certain correlation window and the resulting contrast for the focal spot. This is the first theoretical conclusion: the noise correlation method obeys Gabor information theory: it manipulates time-information grains.

B. What is the lowest reachable correlation window?

With the Gabor information approach validated, we now tackle the second key-question: what is the shortest usable correlation window? For the central wavelength to be measurable at a certain spatial location, a focal spot has to be reconstructed. For this purpose, enough time-information grains must be contained in the correlation window to retrieve a local maximum at the chosen point. Hence, in 1D, the standard deviation of a sinusoidal function being $1/\sqrt{2}$, the correlation contrast must be larger than $\sqrt{2}$. Similarly, in 2D we must have $\gamma_{corr} > \sqrt{2}^2 = 2$ and $\gamma_{corr} > \sqrt{2}^3 = 2\sqrt{2}$ in 3D. Since $\gamma_{corr}^2 = \Delta t \Delta f$, for a certain frequency bandwidth, the shortest correlation window allowing to calculate a focal spot is given by:

$$\begin{cases} \Delta t > \frac{\sqrt{2}^2}{\Delta f} = \frac{2}{\Delta f} \; in \; 1D \\ \Delta t > \frac{2^2}{\Delta f} = \frac{4}{\Delta f} \; in \; 2D \\ \Delta t > \frac{(2\sqrt{2})^2}{\Delta f} = \frac{8}{\Delta f} \; in \; 3D \end{cases}$$

Therefore, in the 2D elastic simulation previously presented, the frequency bandwidth being around 600 Hz, the shortest correlation window that can be used to retrieve a focal spot at all points is $\Delta t = \frac{4}{\Delta f} = \frac{4}{600} = 6.6\, ms$, which corresponds to a frame rate of 150 Hz. Hence, the 3 time-steps correlation window is even shorter (3 ms) than the theoretical shortest time. Indeed, in fig.4(d) it can be seen that the exact wave speed is not well retrieved at all points since a focal spot can not be retrieved for all points. In the end, when averaging along the image width (fig.4(f)) the speed contrast as a function of depth is conserved, but quantitative wave speed imaging is barely possible.

C. Perspectives: implications for real-time imaging and monitoring

In clinically used methods such as ARFI in combination with time-of-flight, a minimum acquisition time corresponding to a minimum wavefront propagation length are required to estimate the shear wave speed. If a magneto-motive elastography method were to be used in combination with noise correlation algorithms, only a few time steps could be used to detect elasticity contrasts. Indeed, magnetic nano-particles are already widely used *in vivo* as contrast agents in magnetic resonance imaging [20, 21], are emerging in the field of magnetic particle imaging [22], and have been used for magneto-motive ultrasound imaging (MMUS) [24, 42, 43]. Hence, our experiment shows that the clinical use of real-time magneto-motive elastography is realistic and could unlock real-time elasticity estimation.

V. CONCLUSION

To conclude, we experimentally realized diffuse elastic fields *in situ* through the combination of a magnetic pulser and magnetic particles. Our 3d laboratory realization, 2d numerical experiment, and theoretical considerations show that only a few discrete time steps are required to retrieve an elasticity contrast for noise correlation under ideal conditions. A direct imaging application is elasticity characterization in the medical field. Our proof-of-concept experiment suggests that cross-correlation imaging in real-time, as demanded by physicians, is becoming feasible. The same nano-particles which are already used for cancer treatment and MRI have the potential to create diffuse wave-fields for real-time treatment monitoring.

In principle, our findings are applicable to any wave-field correlation method that uses a dense array of receivers to image medium contrasts, such as distributed acoustic sensing, digital image correlation, dense array seismology, or non-destructive testing.

ACKNOWLEDGMENTS

The project has received funding from the Plan Cancer Arc-2018-PhysiCancer-Bpalp and the Swiss National Foundation under the grant No 197182. With financial support from ITMO Cancer of Aviesan within the framework of the 2021-2030 Cancer Control Strategy, on funds administered by Inserm.

Appendix: Comparison with a gold standard: Acoustic Radiation Force Impulse - Shear Wave Elastography

As a ground truth elasticity measurement, we implemented acoustic radiation force shear wave elastography (ARFI-SWE) in the phantom of fig.1. In ARFI-SWE, the focusing of ultrasonic waves in a point in the medium of interest creates a force which in turn acts as a shear wave source. Immediately after the shear wave generation, the same plane wave imaging sequence, as in the diffuse field experiment, was used. Then, the shear wave field was retrieved using the same phase-based motion estimator. The three exemplary displacement snapshots in figure 5(a) show a shear wave front

originating from the focusing of ultrasonic beams at a depth of 25 mm and in the lateral centre of the probe. It can already be seen that the wave front propagates faster in the bottom than in the top layer. Next, we applied equation 1 to the ARFI-SWE displacements. The resulting shear wave velocity map displayed in figure 5(b) shows a clear velocity contrast between the two layers, except on the wave source location (central vertical line). Finally, a classical time-of-flight algorithm [44] was used for comparison. In figure 5(c) the velocity profiles are plotted as a function of depth, obtained using either noise correlation or time-of-flight. Both algorithms retrieve a sharp velocity increase at 22 mm depth, in accordance with fig. 2. The profile obtained using correlation is smoother than the time-of-flight profile, but they quantitatively agree (RMS $\simeq 0.15\,\mathrm{m\,s^{-1}}$). This corroborates the measurements showing the different elasticities of the bi-layered gel phantom. However, the shear wave speeds differ from the previous results. This may be due to either, the difference in the frequency content leading to dispersion in viscoelastic media or the presence of a measurement noise. This noise may impact the focal spot when noise correlation approaches are performed in other sections. This phenomenon can be observed in seismology [45].

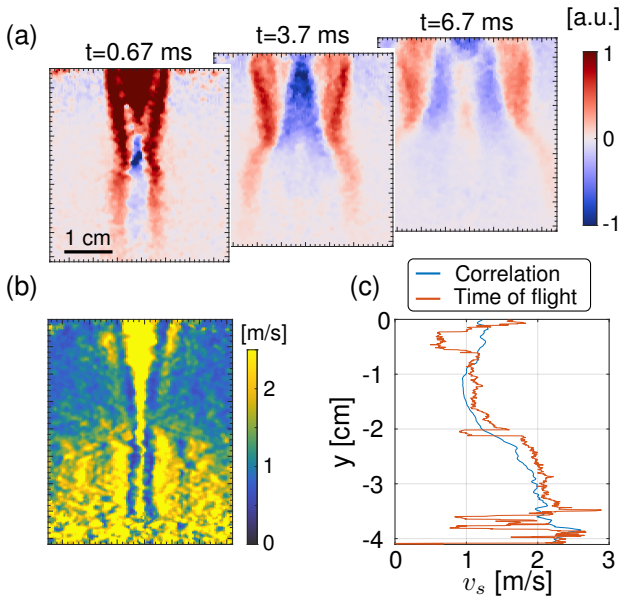

FIG. 5. **Ultrasonic push (ARFI) results.** (a) Snapshots of the displacement film at three times. (b) Shear wave velocity map retrieved using passive elastography algorithms. (c) Velocity profiles as a function of depth retrieved by averaging the shear wave velocity map in (b) and measuring the time-of-flight.

[1] D. Ayala-Garcia, A. Curtis, and M. Branicki, Seismic Interferometry from Correlated Noise Sources, Remote Sensing **13**, 2703 (2021).

[2] D.-J. van Manen, J. O. A. Robertsson, and A. Curtis, Modeling of Wave Propagation in Inhomogeneous Media, Physical Review Letters **94**, 164301 (2005).

[3] M. Campillo and A. Paul, Long range correlations in the diffuse seismic coda, Science **299**, 547 (2003).

[4] A. Sergeant, M. Chmiel, F. Lindner, F. Walter, P. Roux, J. Chaput, F. Gimbert, and A. Mordret, On the Green's function emergence from interferometry of seismic wave fields generated in high-melt glaciers: Implications for passive imaging and monitoring, The Cryosphere **14**, 1139 (2020).

[5] J. Spytek, L. Pieczonka, T. Stepinski, and L. Ambrozinski, Mean local frequency-wavenumber estimation through synthetic time-reversal of diffuse lamb waves, Mech. Syst. Signal Process **156**, 107712 (2021).

[6] L. Eisner, P. M. Duncan, W. M. Heigl, and W. R. Keller, Uncertainties in passive seismic monitoring, The Leading Edge **28**, 648 (2009).

[7] T. Gallot, S. Catheline, P. Roux, J. Brum, N. Benech, and C. Negreira, Passive elastography: Shear-wave tomography from physiological-noise correlation in soft tissues, IEEE Trans. Ultrason. Ferroelectr. Freq. Control **58**, 1122 (2011).

[8] S. Catheline, R. Souchon, M. Rupin, J. Brum, A. H. Dinh, and J. Y. Chapelon, Tomography from diffuse waves: Passive shear wave imaging using low frame rate scanners, Appl. Phys. Lett. **103**, 10.1063/1.4812515 (2013).

[9] A. Zorgani, R. Souchon, A.-H. Dinh, J.-Y. Chapelon, J.-M. Ménager, S. Lounis, O. Rouvière, and S. Catheline, Brain palpation from physiological vibrations using mri, Proc. Natl. Acad. Sci. USA **112**, 12917 (2015).

[10] T.-M. Nguyen, A. Zorgani, M. Lescanne, C. Boccara, M. Fink, and S. Catheline, Diffuse shear wave imaging: Toward passive elastography using low-frame rate spectral-domain optical coherence tomography, Journal of Biomedical Optics **21**, 126013 (2016).

[11] P. Grasland-Mongrain, A. Zorgani, S. Nakagawa, S. Bernard, L. G. Paim, G. Fitzharris, S. Catheline, and G. Cloutier, Ultrafast imaging of cell elasticity with optical microelastography, Proc. Natl. Acad. Sci. USA **115**, 861 (2018).

[12] J. Brum, N. Benech, T. Gallot, and C. Negreira, Shear Wave Elastography Based on Noise Correlation and Time Reversal, Front. Phys. **9**, 10.3389/fphy.2021.617445 (2021).

[13] A. Derode, P. Roux, and M. Fink, Robust acoustic time reversal with high-order multiple scattering, Phys. Rev. Lett. **75**, 4206 (1995).

[14] J. F. Claerbout, Synthesis of a layered medium from its acoustic transmission response, Geophysics **33**, 264 (1968).

[15] R. L. Weaver, On diffuse waves in solid media, J. Acoust. Soc. Am. **71**, 1608 (1982).

[16] R. L. Weaver and O. I. Lobkis, Ultrasonics without a source: Thermal fluctuation correlations at mhz frequencies, Phys. Rev. Lett. **87**, 1 (2001).

[17] A. Hejazi Nooghabi, L. Boschi, P. Roux, and J. de Rosny, Coda reconstruction from cross-correlation of a diffuse field on thin elastic plates, Physical Review E **96**, 032137 (2017).

[18] K. Wapenaar, J. Fokkema, and R. Snieder, Retrieving the Green's function in an open system by cross correlation: A comparison of approaches (L), The Journal of the Acoustical Society of America **118**, 2783 (2005).

[19] A. C. Prunty, R. K. Snieder, and C. Sens-Schönfelder, Acoustic imaging using unknown random sources, The Journal of the Acoustical Society of America **149**, 499 (2021).

[20] S. Mornet, S. Vasseur, F. Grasset, P. Veverka, G. Goglio, A. Demourgues, J. Portier, E. Pollert, and E. Duguet, Magnetic nanoparticle design for medical applications, Progress in Solid State Chemistry **34**, 237 (2006).

[21] C. Fang and M. Zhang, Multifunctional magnetic nanoparticles for medical imaging applications, Journal of Materials Chemistry **19**, 6258 (2009).

[22] J. Borgert, J. D. Schmidt, I. Schmale, J. Rahmer, C. Bontus, B. Gleich, B. David, R. Eckart, O. Woywode, J. Weizenecker, J. Schnorr, M. Taupitz, J. Haegele, F. M. Vogt, and J. Barkhausen, Fundamentals and applications of magnetic particle imaging, Journal of Cardiovascular Computed Tomography **6**, 149 (2012).

[23] A. Farzin, S. A. Etesami, J. Quint, A. Memic, and A. Tamayol, Magnetic nanoparticles in cancer therapy and diagnosis, Advanced healthcare materials **9**, e1901058 (2020).

[24] M. Mehrmohammadi, T.-H. Shin, M. Qu, P. Kruizinga, R. L. Truby, J.-H. Lee, J. Cheon, and S. Y. Emelianov, In vivo pulsed magneto-motive ultrasound imaging using high-performance magnetoactive contrast nanoagents, Nanoscale **5**, 11179 (2013).

[25] T. Z. Pavan, D. R. T. Sampaio, A. A. O. Carneiro, and D. T. Covas, Ultrasound-based transient elastography using a magnetic excitation, in *2012 IEEE International Ultrasonics Symposium* (2012) pp. 1846–1849.

[26] G. Laloy-Borgna, L. Vovard, A. Rohfritsch, L. Wang, J. Ngo, M. Perier, A. Drainville, F. Prat, M. Lafond, C. Lafon, and S. Catheline, Magnetic microelastography for evaluation of ultrasound-induced softening of pancreatic cancer spheroids, Phys. Rev. Appl. **22**, 024024 (2024).

[27] Z. Sun, B. Giammarinaro, A. Birer, G. Liu, and S. Catheline, Shear Wave Generation by Remotely Stimulating Aluminum Patches with a Transient Magnetic Field and its Preliminary Application in Elastography, IEEE Transactions on Biomedical Engineering **68**, 2129 (2021).

[28] J. R. Morillas and J. de Vicente, Magnetorheology: A review, Soft Matter **16**, 9614 (2020).

[29] M. Tanter and M. Fink, Ultrafast imaging in biomedical ultrasound, IEEE Trans. Ultrason. Ferroelectr. Freq. Control **61**, 102 (2014).

[30] G. Pinton, J. Dahl, and G. Trahey, Rapid Tracking of Small Displacements with Ultrasound, in *IEEE Ultrasonics Symposium, 2005.*, Vol. 4 (IEEE, 2005) pp. 2062–2065.

[31] N. Benech, J. Brum, S. Catheline, T. Gallot, and C. Negreira, Near-field effects in Green's function retrieval from cross-correlation of elastic fields: Experimental study with application to elastography, J. Acoust. Soc. Am. **133**, 2755 (2013).

[32] C. Zemzemi, A. Zorgani, L. Daunizeau, S. Belabhar, R. Souchon, and S. Catheline, Super-resolution limit of shear-wave elastography, Europhys. Lett. **129**, 34002 (2020).

[33] A. Marmin, S. Catheline, and A. Nahas, Full-field passive elastography using digital holography, Opt. Lett., OL **45**, 2965 (2020).

[34] G. Laloy-Borgna, A. Zorgani, and S. Catheline, Microelastography: Toward ultrasonic shear waves in soft solids, Appl. Phys. Lett. **118**, 113701 (2021).

[35] S. Catheline, J. L. Gennisson, G. Delon, M. Fink, R. Sinkus, S. Abouelkaram, and J. Culioli, Measuring of viscoelastic properties of homogeneous soft solid using transient elastography: An inverse problem approach., J. Acoust. Soc. Am. **116**, 3734 (2004).

[36] M. Afanasiev, C. Boehm, M. van Driel, L. Krischer, M. Rietmann, D. A. May, M. G. Knepley, and A. Fichtner, Modular and flexible spectral-element waveform modelling in two and three dimensions, Geophys. J. Int. **216**, 1675 (2019).

[37] D. Gabor, Theory of communication. Part 1: The analysis of information, Journal of the Institution of Electrical Engineers - Part III: Radio and Communication Engineering **93**, 429 (1946).

[38] D. Gabor, Communication theory and physics, Transactions of the IRE Professional Group on Information Theory **1**, 48 (1953).

[39] D. Gabor, The transmission of information by coherent light. I. Classical theory, J. Phys. E: Sci. Instrum. **8**, 73 (1975).

[40] D. Gabor, IV Light and Information, in *Progress in Optics*, Vol. 1, edited by E. Wolf (Elsevier, 1961) pp. 109–153.

[41] M. Franceschetti, *Wave Theory of Information* (Cambridge University Press, Cambridge, 2017).

[42] J. Oh, M. D. Feldman, J. Kim, C. Condit, S. Emelianov, and T. E. Milner, Detection of magnetic nanoparticles in tissue using magneto-motive ultrasound, Nanotechnology **17**, 4183 (2006).

[43] Y. Hadaian, D. R. T. Sampaio, A. P. Ramos, A. A. O. Carneiro, and T. Z. Pavan, Magneto-motive ultrasound imaging using superparamagnetic ferrite nanoparticle with enhanced saturation magnetization synthesized by a simple copreciptation method, in *2017 IEEE International Ultrasonics Symposium (IUS)* (2017) pp. 1–4.

[44] J.-L. Gennisson, T. Deffieux, M. Fink, and M. Tanter, Ultrasound elastography: Principles and techniques, Diagnostic and Interventional Imaging **94**, 487 (2013).

[45] B. Giammarinaro, C. Tsarsitalidou, G. Hillers, J. de Rosny, L. Seydoux, S. Catheline, M. Campillo, and P. Roux, Seismic surface wave focal spot imaging: Numerical resolution experiments, Geophys. J. Int. **232**, 201 (2023).